PHOTONICS Research

Visible Raman and Brillouin lasers from a microresonator/ZBLAN-fiber hybrid system

Shuisen Jiang, Changlei Guo, Kaijun Che, Zhengqian Luo, Tuanjie Du, Hongyan Fu, Huiying Xu, and Zhiping Cai*

Department of Electronic Engineering, Xiamen University, Xiamen 361005, China
**Corresponding author: zpcai@xmu.edu.cn*

Received 8 November 2018; revised 6 January 2019; accepted 13 March 2019; posted 14 March 2019 (Doc. ID 351318); published 29 April 2019

Raman and Brillouin lasers based on a high-quality (high-Q) whispering gallery mode microresonator (WGMR) are usually achieved by employing a tunable single-frequency laser as a pump source. Here, we experimentally demonstrate visible Raman and Brillouin lasers using a compact microresonator/ZrF_4–BaF_2–LaF_3–AlF_3–NaF (ZBLAN)-fiber hybrid system by incorporating a WGMR with a fiber-compatible distributed Bragg reflector/fiber Bragg grating to form a Fabry–Perot (F-P) fiber cavity and using a piece of Pr:ZBLAN fiber as gain medium. The high-Q silica-microsphere not only offers a Rayleigh-scattering-induced backreflection to form the ∼635 nm red laser oscillation in the F-P fiber cavity, but also provides a nonlinear gain in the WGMR itself to generate either stimulated Raman scattering or stimulated Brillouin scattering. Up to six-order cascaded Raman lasers at 0.65 μm, 0.67 μm, 0.69 μm, 0.71 μm, 0.73 μm, and 0.76 μm are achieved, respectively. Moreover, a Brillouin laser at 635.54 nm is clearly observed. This is, to the best of our knowledge, the first demonstration of visible microresonator-based lasers created by combining a Pr:ZBLAN fiber. This structure can effectively extend the laser wavelength in the WGMR to the visible waveband and may find potential applications in underwater communication, biomedical diagnosis, microwave generation, and spectroscopy.

https://doi.org/10.1364/PRJ.7.000566

1. INTRODUCTION

Benefiting from high-quality (high-Q)-factor resonance and low mode volume (V), the light–matter interaction with a figure of merit Q/V can be significantly enhanced in whispering gallery mode microresonators (WGMRs) [1]. Many applications or scientific studies, such as low-threshold microlasers, highly sensitive optical detection, optomechanics, and nonlinear optics, have been widely explored in recent decades [2–6]. In particular, stimulated nonlinear phenomena, such as stimulated Raman scattering (SRS) [7–16], stimulated Brillouin scattering (SBS) [17–19], and four-wave mixing [20–23], have been achieved in WGMRs under an ultra-low-threshold pumping. As a natural nonlinear optical phenomenon [24], Raman scattering could extend the laser waveband significantly. As early as 1985, the visible Raman lasing in an individual liquid droplet with a radius of ∼30 μm was demonstrated [7], and then the Vahala group reported SRS at the near-infrared (IR) waveband in a silica microsphere with a threshold power as low as 50 μW [8]. Up to this point, SRS has been extensively achieved in sphere/disk/toroid/bottle-like microresonators with different hold media [8–16]. Benefiting from the ultra-narrow linewidth, Raman lasing in WGMRs has recently been explored for non-label nanoparticle sensing in both aqueous environments and air [25–27]. In addition, SBS in WGMRs has a wide range of applications, such as microwave generation [28,29], nonreciprocal light storage [30,31], and high coherence microlasers [32].

Visible high-coherence lasers have become more and more attractive in recent years due to their important roles in underwater communication, biomedical diagnosis, and microscopy. However, even though there are a few reports on the study of nonlinear optics in WGMRs in the visible waveband [12,16,21,22], resorting to external tunable single-frequency lasers (TSFLs) as pump sources, visible Raman and Brillouin lasers are still not adequately explored to fulfill future applications. In particular, Brillouin lasers in WGMRs have not (to our knowledge) been demonstrated in the visible waveband so far. There are two cost-effective ways to replace external TSFLs for pumping WGMRs. One is to combine rare-earth-doped fibers [33–35] as a gain medium, and the other is to use semiconductor chips [36]. In the first scheme, erbium (Er)- and ytterbium (Yb)-doped silica fibers have been used to explore single-frequency lasers and further nonlinear optical phenomena in the near-IR range. However, due to the high phonon energy in silica fibers, rare-earth ions lose activity in the visible waveband. One effective way to solve this problem

is to resort to low-phonon energy fibers such as a ZrF_4–BaF_2–LaF_3–AlF_3–NaF (ZBLAN) fiber. During the past few years, praseodymium-doped ZBLAN (Pr:ZBLAN) fiber lasers have been fully studied in the visible range [37–39], but visible SRS and SBS have not yet been experimentally demonstrated in either ZBLAN fibers or conventional silica fibers. Here, by combining the high gain of Pr:ZBLAN fiber in the visible waveband, especially at ~635 nm, with high-Q WGMRs for nonlinear optics, visible Raman and Brillouin lasers are achieved.

In this paper, we demonstrate for the first time, to the best of our knowledge, a compact visible fiber laser enabling Raman and Brillouin lasing by employing a structure that combines a microresonator with a piece of Pr:ZBLAN fiber, instead of using a TSFL as pump source. Moreover, a visible Brillouin laser in a WGMR is demonstrated. The high-Q microresonator (here, silica microsphere) is employed not only as a mode reflector for the fiber lasing but also as a nonlinear initiator for the production of SRS or SBS. Fiber-lasing-pumped, microresonator-initiated, up to six-order-cascaded Raman lasers at 0.65 μm, 0.67 μm, 0.69 μm, 0.71 μm, 0.73 μm, and 0.76 μm, as well as a first-order Brillouin laser at 635.54 nm, are realized.

2. OPERATION PRINCIPLES AND EXPERIMENTAL SETUP

The experimental setup of the proposed microresonator/ZBLAN-fiber hybrid system is schematically shown in Fig. 1(a). A GaN laser diode (LD) emitting at ~444 nm with a maximum output of ~2 W is employed as the pump source, and a 91.5 cm Pr:ZBLAN fiber (core/cladding = 6/125 μm, NA = 0.15, Pr^{3+} concentration = 0.1%) is used as the gain medium. The Fabry–Perot (F-P) fiber cavity is composed of an input mirror and a fiber taper coupled silica microsphere (as the output mirror). The total fiber cavity length is ~4.2 m. A fiber polarization controller (FPC; FPC-100, OZ Optics) is used inside the fiber cavity for optimizing the polarization states. In this hybrid laser system, two kinds of input mirrors are used, separately. The first is a homemade end-facet mirror [fiber-compatible distributed Bragg reflector (DBR)] labeled M1, which is fabricated by directly coating multilayer SiO_2/Ta_2O_5 dielectric thin films onto a single-mode-fiber (SMF; 1060-XP) end-facet using a plasma sputter deposition system (SCTS500, System Control Technologies, Inc.). The second is a commercial fiber Bragg grating (FBG). Because the Pr:ZBLAN fiber has the strongest gain at ~635 nm ($^3P_0 \rightarrow {}^3F_2$ transition) in the visible waveband, both input mirrors select ~635 nm as the center wavelength for the demonstration. Figure 1(b) shows the transmission spectrum of the homemade end-facet mirror, where the transmittance is ~76.8% at an ~444 nm pump wavelength and the reflectivity is ~95.7% at the designed wavelength of 635 nm. Furthermore, mirror M1 has a high reflection in the visible waveband ranging from 500 to 700 nm. The insets in Fig. 1(b) show the photograph (left) and microscopic image (right) of M1. The FBG (O/E Land Inc.) has a center wavelength located at 635.4 nm, with a high reflectivity of >99% and a 3 dB bandwidth of 0.3 nm. A microscopic image of the silica microsphere employed in our experiment is shown in Fig. 1(c); it is fabricated by melting a standard silica fiber (Corning SMF-28) tip using a CO_2 laser and has a diameter of ~152 μm. A fiber taper with a diameter of 1–2 μm serves as a coupler for coupling light into and out of the microsphere. Due to the lack of a ~0.63 μm TSFL in our laboratory, the Q-factor of the microsphere around 0.63 μm cannot be measured directly. In order to evaluate the quality of the fabricated microresonator, the Q-factor of the microsphere at around 1550 nm is measured, which is $\sim 1.3 \times 10^8$ as used in our experiment. The reflection ratio from the microsphere, which is determined by Rayleigh-scattering-induced modal coupling between clockwise and counterclockwise WGMs [40–42] is also measured with the help of an optical circulator (the method is shown in our previous publication [43]). In this work, the reflection ratio is approximately 20%–30% in the over-coupling regime [44], when the fiber taper touches the microresonator to reduce perturbation from the environment. The microsphere and the DBR/FBG mirror work together to form an F-P cavity, which provides the principal laser oscillation with a threshold of $P_{\text{threshold}} = K(\alpha - \ln R_1 R_2)$ [45], where K is a constant scaling factor that is related to the fluorescence quantum efficiency, gain saturation coefficient, Pr:ZBLAN fiber core radius, etc.; α represents the total pump losses including the Pr:ZBLAN fiber absorption and other fiber absorption and connection losses; R_1 and R_2 are the DBR/FBG mirror and microsphere reflection ratios, respectively. Based on the theoretical calculation, the semi-quantitative relationship between $P_{\text{threshold}}[K(W)]$ and R_2 is shown in Fig. 2 using DBR M1 ($R_1 = 95.7\%$, blue solid line) or the FBG ($R_1 = 99\%$, red dashed line) as the input mirror, where α is 0.999, considering a total cavity loss of 30 dB. In our experiments, once the pump power is beyond the threshold, the principal laser around 635 nm is first observed, and the inset in Fig. 1(a) is a photograph of the output laser spot.

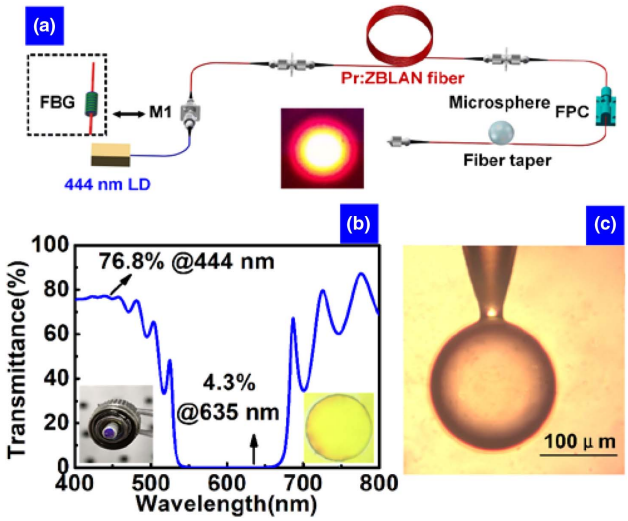

Fig. 1. (a) Experimental setup for the microresonator/ZBLAN-fiber hybrid system. Inset: photograph of the output light spot in our experiment. (b) Optical transmission spectrum of the fiber end-facet mirror M1. Insets: photograph (left) and microscopic image (right) of M1. (c) A microscopic image of the silica microsphere used in the experiment.

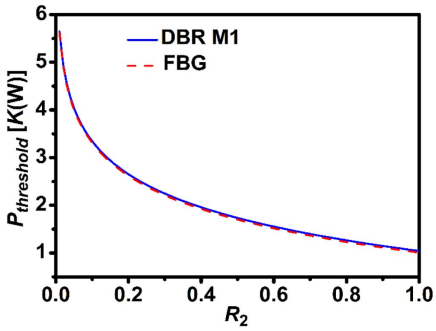

Fig. 2. Semi-quantitative relationship between $P_{\text{threshold}}[K(W)]$ and R_2 using DBR M1 ($R_1 = 95.7\%$, blue solid line) or the FBG ($R_1 = 99\%$, red dashed line) as the input mirror.

3. EXPERIMENTAL RESULTS AND DISCUSSION

The first scheme is performed with a fiber-compatible DBR M1 as the input mirror. Figures 3(a) and 3(b) show the emission spectra from the output port [see Fig. 1(a)] with and without a microsphere as the feedback element, respectively. The fluorescence peaks at ~605 nm, ~635 nm, and ~719 nm in Fig. 3(b) correspond to the $^3P_0 \rightarrow {}^3H_6$, $^3P_0 \rightarrow {}^3F_2$, and $^3P_0 \rightarrow {}^3F_4$ transitions, respectively, as shown by the inset energy level in Fig. 3(b). And the green dashed line in the inset in Fig. 3(b) illustrates the fast nonradiative relaxation between $^3P_2$ and $^3P_0$. In comparison with Fig. 3(b), the lasing modes are obviously formed at ~635 nm in Fig. 3(a), and the fluorescences at ~605 nm and ~719 nm have been suppressed by more than 30 dB compared with the lasing modes. Here, the ~444 nm laser pump power is ~263 mW, and the ~635 nm laser output power is about 4.5 mW. As depicted in the inset in Fig. 3(a), the laser emission at ~635 nm exhibits a multimode [optical spectrum analyzer (OSA), 0.01 nm resolution] characteristic. This might be due to the fact that mirror M1 has a wide reflection bandwidth at ~0.63 μm in Fig. 1(b), which could support a larger number of cavity modes to be initiated at the same time. Moreover, the threshold pump power at ~444 nm is estimated to be ~213 mW. When the pump power is increased no more than 345 mW, Raman lasing is not available and the ~635 nm laser output power is up to ~6.8 mW.

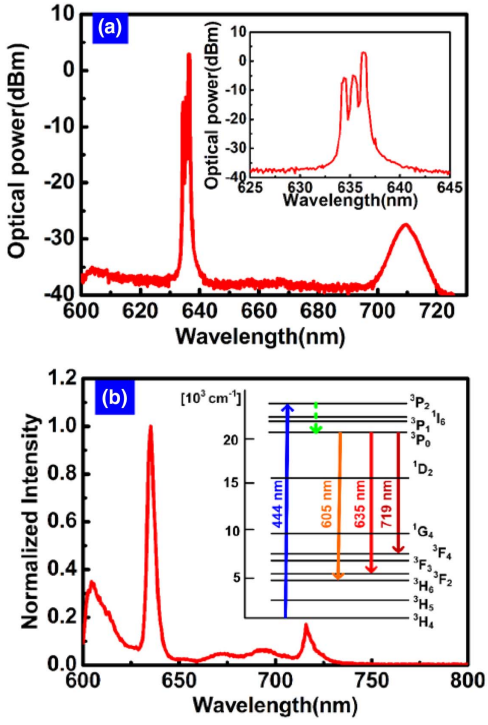

Fig. 3. (a) Laser output spectrum under a pump power of ~263 mW. Inset: detailed optical spectrum at ~635 nm. (b) Fluorescence spectrum from the output port without a microsphere as the feedback element. Inset: a partial energy level diagram of Pr^{3+} ions in the ZBLAN fiber.

In order to further realize SRS, a nonlinear optical process that transfers energy from a pump wave to Stokes and anti-Stokes waves through optical phonons [24], in the hybrid laser system, the ~444 nm pump power is increased further. By optimizing the fiber polarization as well as the fiber taper/microresonator coupling condition, SRS is realized once the newly generated ~635 nm laser is beyond the SRS lasing threshold. As shown in Figs. 4(a)–4(f), the spectra of one- to six-order Raman Stokes lasers are measured (OSA, 0.01 nm resolution) with a ~444 nm pump power of 347, 359, 385, 446, 558, and 603 mW, respectively. Note that each order of Raman Stokes lasers shows multimode characteristics, which might be due to the multimode pumping from the ~635 nm. A broad Raman gain, together with a small free spectral range (FSR) of the microsphere, also helps to lead the multimode lasing. As depicted in Fig. 4(f), the center wavelengths of the first-, second-, third-, fourth-, fifth-, and sixth-order Raman Stokes lasers are located at 654.7, 675.7, 694.8, 715.0, 738.4, and 761.4 nm, respectively. The Raman frequency shifts (RFSs) between adjacent order Stokes lasers can be calculated by the formula $\Delta\nu = c/\lambda_n - c/\lambda_{n+1}$. A spectral line located at 635.7 nm is chosen as the pump light to calculate the RFSs. The cascaded RFSs are about 13.8, 14.1, 12.3, 12.0, 13.5, and 12.3 THz, respectively. The RFSs are different because silica has a large Raman gain bandwidth ranging from 0 to 40 THz [46], and the Raman gain peak in silica is mainly located from 12 to 15 THz. The measured RFSs here are in good agreement with this range, proving that it is the silica microsphere and not the ZBLAN fiber that leads to the observed Raman shifts.

The Raman Stokes laser thresholds in microresonators have been studied both theoretically and experimentally in Refs. [9,13], where a TSFL is utilized. Based on the theory [9,13], the Raman Stokes laser threshold has cubic dependence on the order of Raman emission. In addition, odd-order Raman Stokes power increases proportionally to the square root of the pump power, whereas the even-order Raman Stokes power varies linearly with the pump power. In our experiments, because of the lack of a wavelength discrimination element such as WDM to separate the ~635 nm laser and each order of Raman Stokes laser, the Raman Stokes laser threshold for each order is estimated by observing the full spectra on the OSA, as shown in Fig. 4. The threshold pump power from the 444 nm laser is recorded when each order of Raman Stokes laser is first

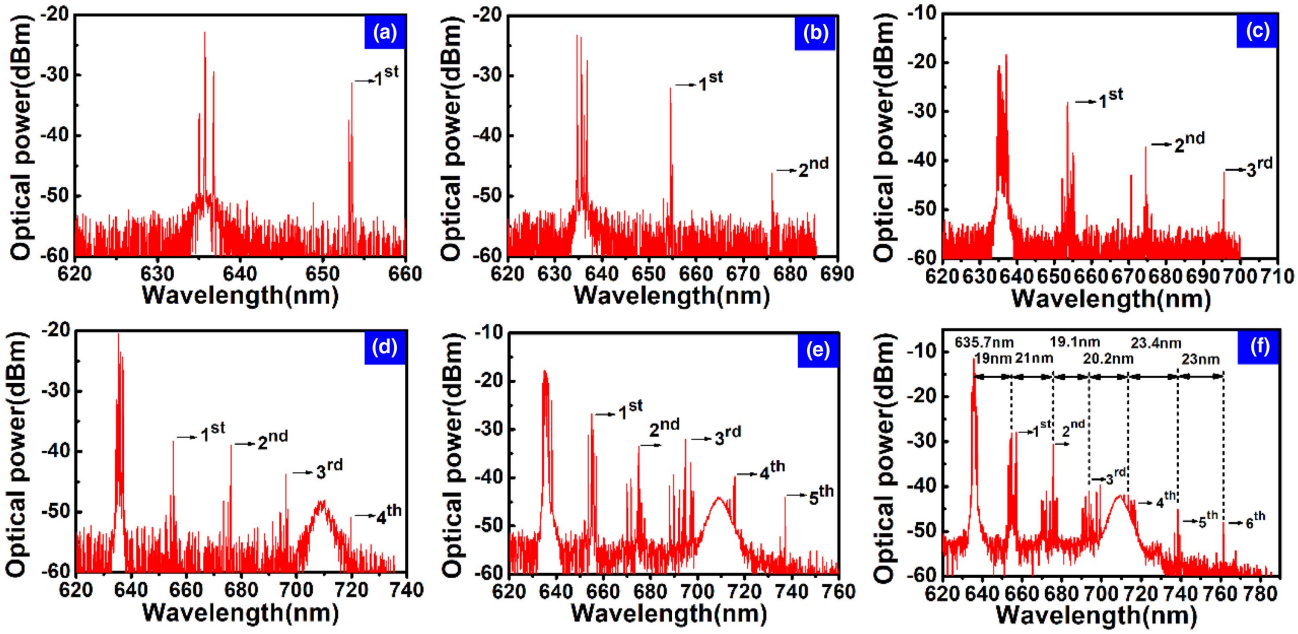

Fig. 4. (a)–(f) One- to six-order Raman Stokes laser spectra in the visible band under pump powers of 347, 359, 385, 446, 558, and 603 mW, respectively.

observed on the OSA. Using this method, the thresholds for the Raman Stokes laser orders are estimated to be 345, 352, 373, 427, 506, and 593 mW, respectively. The threshold power versus the Stokes order is shown in Fig. 5, in which one can see that the cascaded Raman Stokes threshold increases at a cubic rate that is proportional to the Raman Stokes order number. It agrees well with the theoretical results reported in Refs. [9,13]. And the result illustrates that the pump powers of the higher-order Raman Stokes lasers are relatively large. The reason might be that the Raman gain coefficient is inversely proportional to the pump wavelength [13]. Even though the Raman Stokes thresholds here are higher than those given in Ref. [13], where a TSFL could improve the pumping efficiency, compared with the SRS threshold power in a pure fiber laser [47], the microspheres with a high Q-factor and low mode volume have significantly lower threshold power. Moreover, the first-order Raman Stokes laser power versus pump power is shown in Fig. 6(a), and it follows a square root dependency as expected [9,13]. Figure 6(b) shows the second-order Raman Stokes laser power versus pump power. The growth of the second-order Raman Stokes laser also follows the expected linear dependency as the pump power increases [9,13]. It is worth noting that because of the multimode lasing characteristics in Fig. 3(a) and Figs. 4(a)–4(f), the Brillouin spectra are not easy to identify. Thus, the Brillouin effect is not specially studied in the DBR scheme.

Next, the second scheme with the FBG as the input mirror is implemented. The Raman laser failed to be generated in this scheme. However, by increasing the pump power, finely optimizing the polarization states, and controlling the coupling position between the fiber taper and the microsphere, the Brillouin laser was realized successfully. Even though SBS and its applications have been fully explored in the IR range within WGMRs, this interesting nonlinear phenomenon, which originates from the electrostriction effect, has never been explored in the visible waveband to our knowledge. When a pump photon is annihilated, a redshifted Stokes photon and an acoustic phonon are generated simultaneously [24]. Moreover, the frequency of the acoustic phonon can be theoretically

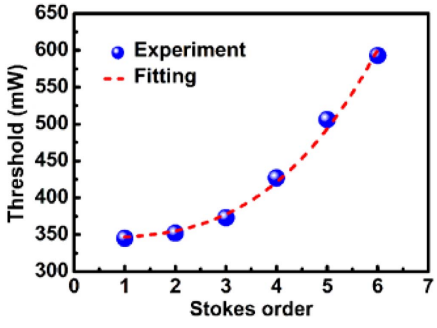

Fig. 5. Threshold power dependence on the Raman Stokes order. Blue dots: experimental data. Red dashed line: cubic fitting.

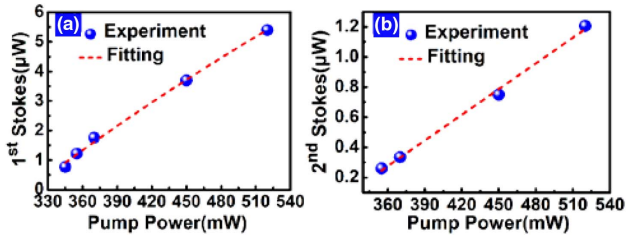

Fig. 6. (a) First-order Raman Stokes laser power versus pump power. Blue dots: experimental data. Red dashed line: square root fitting. (b) Second-order Raman Stokes laser power versus pump power. Blue dots: experimental data. Red dashed line: linear fitting.

defined as $\Delta\nu_B = 2nV_A/\lambda_S$ [also know as the Brillouin frequency shift (BFS)], where n is the refractive index of the medium, V_A is the acoustic velocity in the medium, and λ_S is the working wavelength. It is worth noting that the frequency of the acoustic phonon is inversely related to the working wavelength, which means the phonon energy in the visible waveband is much more than that in the IR range. In our condition, when $n = 1.45$, $V_A = 5.96$ km/s, and $\lambda_S = 635.5$ nm, the calculated $\Delta\nu_B$ is ~27 GHz. Thus, the visible Brillouin lasers with low power consumption and miniature size would be helpful for generating higher frequency microwave signals [28,29,34] and longer non-reciprocal light storage [30,31].

Because the fundamental FSR of a microsphere ranges from hundreds of gigahertz to terahertz, in order to match this ~27 GHz BFS, the high-order (radial or polar) WGMs must be used as the lasing modes. As shown in Fig. 7(a), the single-wavelength laser at 635.5 nm is first observed (OSA, 0.01 nm resolution) under a pump power of ~280 mW, and then it serves as the pump laser for the Brillouin Stokes lasing. The output power of the single-wavelength laser at ~635.5 nm versus pump power is shown in Fig. 7(b). It can be deduced that the threshold of the single-wavelength laser at ~635.5 nm is 276 mW by linearly fitting the experimental data; the total output power is more than 0.8 mW, and the slope efficiency is ~1.5%. First-order Brillouin Stokes lasing at 635.54 nm is excited when the pump power is increased to ~338 mW, which means the pump threshold for Brillouin Stokes lasing is less than 338 mW. The Brillouin spectra are shown in Fig. 7(c), where the three traces are under pump powers of 338 (green), 350 (pink), and 370 mW (blue). In all three traces, the wavelength shifts from the pump beam are 0.04 nm, corresponding to a frequency shift of ~27 GHz. This coincides with the theoretically predicted BFS of ~27 GHz. Furthermore, the laser

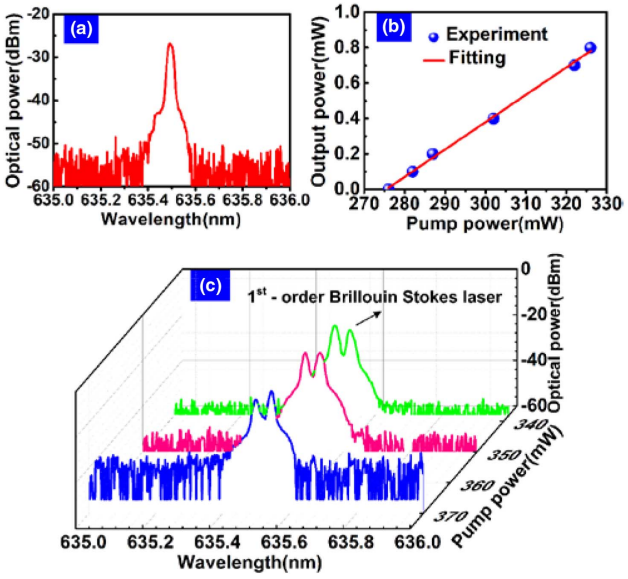

Fig. 7. (a) Spectrum of a single-wavelength laser at 635.5 nm under a pump power of ~280 mW, (b) the output power of the single-wavelength laser at ~635.5 nm versus pump power, (c) Brillouin spectra under different pump powers.

longitudinal mode interval of the fiber F-P cavity is ~24.4 MHz based on the cavity length, which means that the three traces in Fig. 7(c) are not multimode lasers from the fiber F-P cavity. In addition to the spectra in Fig. 7(c), similar spectra with the same frequency shift as the BFS are also observed at other wavelengths. Moreover, the second peak is from buildup by the first one with a certain threshold. All these characteristics lead us to believe that the spectra in Fig. 7(c) result from the Brillouin effect rather than from multimode lasers. Unfortunately, because this BFS is beyond the frequency range of the high-speed photodiodes and microwave spectrum analyzers in our laboratory, currently it cannot be further confirmed by beating the pump and Brillouin Stokes lasers. Interestingly, with the increasing in the pump power from the green trace to the blue trace, as shown in Fig. 7(c), the Brillouin Stokes peak has grown from weak to strong and finally surpasses the pump peak. This is counterintuitive when compared with the phenomena shown in the TSFL-pumped Brillouin Stokes lasers [14,19], where the first-order Brillouin Stokes peak is higher than the peak of the reflected pump in the backward direction, and is lower in the forward direction. The reason might be that the generated Brillouin laser in the backward direction is injected into the F-P fiber cavity and oscillates together with the principal laser. After being amplified by the Pr:ZBLAN fiber, it finally surpasses the principal laser, which is the pump creating the Brillouin effect. It is also worth noting that both the fiber lasing and Brillouin lasing wavelengths in Fig. 7(c) show slight redshifts with increasing pump power. This is mainly due to the thermal-effect-induced WGM frequency shifts in the microsphere [48], which can be used for finely tuning the lasing wavelength in future applications.

In principle, the second scheme can also generate Raman lasers. But due to the fact that the FBG has a very narrow 3 dB linewidth (~0.3 nm), multimode fiber lasing is not realized, which could limit the realization of Raman emission by not reaching proper WGMs. In addition, the cascaded Brillouin laser was not observed, which might be due to either the fact that the second-order Brillouin laser threshold is not reached or that the needed BFS is not fulfilled with a proper WGM.

4. CONCLUSION

In conclusion, a compact microresonator/ZBLAN-fiber hybrid laser system was proposed and experimentally demonstrated. The structure combines a Pr:ZBLAN fiber and a high-Q silica microsphere. A homemade fiber-compatible DBR and a commercial FBG are each used as the input mirror, separately. Benefiting from the gain of Pr:ZBLAN fiber and feedback from the microsphere, a 635 nm red laser is first realized and then used to explore the nonlinear optical effects in the silica microsphere. Cascaded Raman lasers at 0.65 μm, 0.67 μm, 0.69 μm, 0.71 μm, 0.73 μm, and 0.76 μm are achieved in the DBR scheme, while a Brillouin laser at 635.54 nm is realized in the FBG scheme. The nonlinear lasing wavelengths are mainly limited by the first laser from the Pr:ZBLAN fiber, which is balanced by the bandwidth of the input mirror, the feedback signal from the microsphere, and the gain of the Pr:ZBLAN

fiber. Single-mode Raman lasers can be realized by optimizing the fiber taper/microresonator coupling condition in the future. In addition, multi-order Brillouin lasers are expected to be developed by exploring larger microresonators (ideally the ones with fundamental FSRs matching the BFSs). We foresee that this compact structure will become a good platform for future applications as a result of exploring visible Raman and Brillouin lasers.

Funding. National Natural Science Foundation of China (NSFC) (11674269, 91750115).

REFERENCES

1. K. J. Vahala, "Optical microcavities," Nature **424**, 839–846 (2003).
2. L. He, S. Ozdemir, and L. Yang, "Whispering gallery microcavity lasers," Laser Photon. Rev. **7**, 60–82 (2013).
3. J. Zhu, S. Ozdemir, Y. Xiao, L. Li, L. He, D. Chen, and L. Yang, "On-chip single nanoparticle detection and sizing by mode splitting in an ultrahigh-Q microresonator," Nat. Photonics **4**, 46–49 (2010).
4. T. J. Kippenberg and K. J. Vahala, "Cavity optomechanics: back-action at the mesoscale," Science **321**, 1172–1176 (2008).
5. Z. Shen, Z. Zhou, C. Zou, F. Sun, G. Guo, C. Dong, and G. Guo, "Observation of high-Q optomechanical modes in the mounted silica microspheres," Photon. Res. **3**, 243–247 (2015).
6. G. Lin, A. Coillet, and Y. K. Chembo, "Nonlinear photonics with high-Q whispering-gallery-mode resonators," Adv. Opt. Photon. **9**, 828–890 (2017).
7. J. Snow, S. Qian, and R. Chang, "Stimulated Raman scattering from individual water and ethanol droplets at morphology-dependent resonances," Opt. Lett. **10**, 37–39 (1985).
8. S. Spillane, T. J. Kippenberg, and K. J. Vahala, "Ultralow-threshold Raman laser using aspherical dielectric microcavity," Nature **415**, 621–623 (2002).
9. B. Min, T. J. Kippenberg, and K. J. Vahala, "Compact, fiber-compatible, cascaded Raman laser," Opt. Lett. **28**, 1507–1509 (2003).
10. F. Vanier, M. Rochette, N. Godbout, and Y. Peter, "Raman lasing in As_2S_3 high-Q whispering gallery mode resonators," Opt. Lett. **38**, 4966–4969 (2013).
11. F. Vanier, Y. Peter, and M. Rochette, "Cascaded Raman lasing in packaged high quality As_2S_3 microspheres," Opt. Express **22**, 28731–28739 (2014).
12. B. Li, Y. Xiao, M. Yan, W. R. Clements, and Q. Gong, "Low-threshold Raman laser from an on-chip, high-Q, polymer-coated microcavity," Opt. Lett. **38**, 1802–1804 (2013).
13. T. J. Kippenberg, S. M. Spillane, B. Min, and K. J. Vahala, "Theoretical and experimental study of stimulated and cascaded Raman scattering in ultrahigh-Q optical microcavities," IEEE J. Sel. Top. Quantum Electron. **10**, 1219–1228 (2004).
14. G. Lin, S. Diallo, J. M. Dudley, and Y. K. Chembo, "Universal nonlinear scattering in ultra-high Q whispering gallery-mode resonators," Opt. Express **24**, 14880–14894 (2016).
15. T. J. Kippenberg, S. Spillane, D. K. Armani, and K. J. Vahala, "Ultralow-threshold microcavity Raman laser on a microelectronic chip," Opt. Lett. **29**, 1224–1226 (2004).
16. Y. Ooka, Y. Yang, J. Ward, and S. Chormaic, "Raman lasing in a hollow, bottle-like microresonator," Appl. Phys. Express **8**, 092001 (2015).
17. I. Grudinin, A. Matsko, and L. Maleki, "Brillouin lasing with a CaF_2 whispering gallery mode resonator," Phys. Rev. Lett. **102**, 043902 (2009).
18. M. Asano, Y. Takeuchi, S. Ozdemir, R. Ikuta, L. Yang, N. Imoto, and T. Yamamoto, "Stimulated Brillouin scattering and Brillouin-coupled four-wave-mixing in a silica microbottle resonator," Opt. Express **24**, 12082–12092 (2016).
19. C. Guo, K. Che, Z. Cai, S. Liu, G. Gu, C. Chu, H. Fu, Z. Luo, and H. Xu, "Ultralow-threshold cascaded Brillouin microlaser for tunable microwave generation," Opt. Lett. **40**, 4971–4974 (2015).
20. P. Del'Haye, A. Schliesser, O. Arcizet, T. Wilken, R. Holzwarth, and T. J. Kippenberg, "Optical frequency comb generation from a monolithic microresonator," Nature **450**, 1214–1217 (2007).
21. Y. Yang, X. Jiang, S. Kasumie, G. Zhao, L. Xu, J. Ward, L. Yang, and S. Chormaic, "Four-wave mixing parametric oscillation and frequency comb generation at visible wavelengths in a silica microbubble resonator," Opt. Lett. **41**, 5266–5269 (2013).
22. S. Lee, D. Oh, Q. Yang, B. Shen, H. Wang, K. Yang, Y. Lai, X. Yi, X. Li, and K. J. Vahala, "Towards visible soliton microcomb generation," Nat. Commun. **8**, 1295 (2017).
23. J. Ma, X. Jiang, and M. Xiao, "Kerr frequency combs in large-size, ultra-high-Q toroid microcavities with low repetition rates," Photon. Res. **5**, B54–B58 (2017).
24. G. P. Agrawal, *Nonlinear Fiber Optics*, 5th ed. (Academic, 2013).
25. B. Li, W. Clements, X. Yu, K. Shi, Q. Gong, and Y. Xiao, "Single nanoparticle detection using split-mode microcavity Raman lasers," Proc. Natl. Acad. Sci. USA **111**, 14657–14662 (2014).
26. B. Peng, Ş. Özdemir, S. Rotter, H. Yilmaz, M. Liertzer, F. Monifi, C. Bender, F. Nori, and L. Yang, "Loss-induced suppression and revival of lasing," Science **346**, 328–332 (2014).
27. S. Soltani, V. M. Diep, R. Zeto, and A. M. Armani, "Stimulated anti-Stokes Raman emission generated by gold nanorod coated optical resonators," ACS Photon. **5**, 3550–3556 (2018).
28. J. Li, H. Lee, and K. J. Vahala, "Microwave synthesizer using an on-chip Brillouin oscillator," Nat. Commun. **4**, 2097 (2013).
29. J. Li, H. Lee, and K. J. Vahala, "Low-noise Brillouin laser on a chip at 1064 nm," Opt. Lett. **39**, 287–290 (2014).
30. J. Kim, M. Kuzyk, K. Han, H. Wang, and G. Bahl, "Non-reciprocal Brillouin scattering induced transparency," Nat. Phys. **11**, 275–280 (2015).
31. C. Dong, Z. Shen, C. Zou, Y. Zhang, W. Fu, and G. Guo, "Brillouin-scattering-induced transparency and non-reciprocal light storage," Nat. Commun. **6**, 6193 (2015).
32. J. Li, H. Lee, T. Chen, and K. J. Vahala, "Characterization of a high coherence, Brillouin microcavity laser on silicon," Opt. Express **20**, 20170–20180 (2012).
33. K. Kieu and M. Mansuripur, "Fiber laser using a microsphere resonator as a feedback element," Opt. Lett. **32**, 244–246 (2007).
34. S. Jiang, C. Guo, Z. Luo, D. Tang, C. Xiao, C. Ren, K. Che, H. Xu, and Z. Cai, "Cascaded Brillouin, Raman and four-wave-mixing generation in a 1.06 μm microsphere-feedback Yb-fiber laser," IEEE Photon. J. **10**, 1502008 (2018).
35. C. Guo, K. Che, H. Xu, P. Zhang, D. Tang, C. Ren, Z. Luo, and Z. Cai, "Generation of optical frequency combs in a fiber-ring/microresonator laser system," Opt. Lett. **41**, 2576–2579 (2016).
36. W. Liang, V. Ilchenko, D. Eliyahu, A. Savchenkov, A. Matsko, D. Seidel, and L. Maleki, "Ultralow noise miniature external cavity semiconductor laser," Nat. Commun. **6**, 7371 (2015).
37. H. Okamoto, K. Kasuga, I. Hara, and Y. Kubota, "Visible-NIR tunable Pr^{3+}-doped fiber laser pumped by a GaN laser diode," Opt. Express **17**, 20227–20232 (2009).
38. Y. Fujimoto, J. Nakanishi, T. Yamada, O. Ishii, and M. Yamazaki, "Visible fiber lasers excited by GaN laser diodes," Prog. Quantum Electron. **37**, 185–214 (2013).
39. Z. Luo, D. Wu, B. Xu, H. Xu, Z. Cai, F. Wang, Z. Sun, and H. Zhang, "Two-dimensional material-based saturable absorbers: towards compact visible-wavelength all-fiber pulsed lasers," Nanoscale **8**, 1066–1072 (2016).
40. D. Weiss, V. Sandoghdar, J. Hare, V. Lefèvre-Seguin, J. Raimond, and S. Haroche, "Splitting of high-Q Mie modes induced by light backscattering in silica microspheres," Opt. Lett. **20**, 1835–1837 (1995).
41. M. L. Gorodetsky, A. D. Pryamikov, and V. S. Ilchenko, "Rayleigh scattering in high-Q microspheres," J. Opt. Soc. Am. B **17**, 1051–1057 (2000).
42. T. J. Kippenberg, S. M. Spillane, and K. J. Vahala, "Modal coupling in traveling-wave resonators," Opt. Lett. **27**, 1669–1671 (2002).
43. C. Guo, K. Che, P. Zhang, J. Wu, Y. Huang, H. Xu, and Z. Cai, "Low-threshold stimulated Brillouin scattering in high-Q whispering gallery mode tellurite microspheres," Opt. Express **23**, 32261–32266 (2015).

44. S. Spillane, T. J. Kippenberg, O. Painter, and K. J. Vahala, "Ideality in a fiber-taper-coupled microresonator system for application to cavity quantum electrodynamics," Phys. Rev. Lett. **91**, 043902 (2003).
45. A. Yariv, *Quantum Electronics*, 3rd ed. (Wiley, 1989).
46. R. H. Stolen, C. Lee, and R. K. Jain, "Development of the stimulated Raman spectrum in single-mode silica fibers," J. Opt. Soc. Am. B **1**, 652–657 (1984).
47. E. M. Dianov and A. M. Prokhorov, "Medium-power CW Raman fiber lasers," IEEE J. Sel. Top. Quantum Electron. **6**, 1022–1028 (2000).
48. B. Sprenger, H. Schwefel, and L. Wang, "Whispering-gallery-mode-resonator-stabilized narrow-linewidth fiber loop laser," Opt. Lett. **34**, 3370–3372 (2009).